Chemical Engineering Journal Advances 26 (2026) 101065

Contents lists available at ScienceDirect

Chemical Engineering Journal Advances

journal homepage: www.sciencedirect.com/journal/chemical-engineering-journal-advances

Cross-Attention Feature Fusion network for robust estimation of Cd^{2+} and Pb^{2+} in water samples using Cyclic Voltammetry

Rizqy Ahsana Putri [a], Riyanarto Sarno [a],*, Wahyu Prasetyo Utomo [b], Fadlilatul Taufany [c],*, Kelly Rossa Sungkono [a], Taufiq Choirul Amri [a], Alya Kamilah [a], Rini Handayani [a], Sang-Seok Lee [d], A. Min Tjoa [e], Arif Abdullah Sagran [f]

[a] *Department of Informatics, Institut Teknologi Sepuluh Nopember, Surabaya, 60111, Indonesia*
[b] *Department of Chemistry, Institut Teknologi Sepuluh Nopember, Surabaya, 60111, Indonesia*
[c] *Department of Chemical Engineering, Institut Teknologi Sepuluh Nopember, Surabaya, 60111, Indonesia*
[d] *Graduate School of Engineering, Tottori University, Tottori, 680-8552, Japan*
[e] *Department Information Systems Engineering, TU Wien Informatics, Vienna, 1010, Austria*
[f] *Faculdade de Ciências Políticas, Universidade Dili, Dili, 66000, Timor-Leste*

ARTICLE INFO

Keywords:
Cross-attention
Feature fusion
Heavy metal
Improved Beluga Whale Optimization
Voltammetry

ABSTRACT

Voltammetry is a promising technique for estimating heavy metal pollution such as Cadmium (Cd^{2+}) and Lead (Pb^{2+}) in water. Its advantages include rapid analysis and cost-effectiveness over established methods like Atomic Absorption Spectroscopy (AAS) and Inductively Coupled Plasma - Mass Spectrometry (ICP-MS). However, current analysis often depends only on peak data, ignoring the rest of the voltammetric signal which may contain useful information that could potentially improve measurement accuracy. To address this limitation, the Cross-Attention Feature Fusion (CAFF) network is proposed to analyze Cyclic Voltammetry (CV) signals acquired using a 3-electrode setup with a Glassy Carbon Electrode (GCE) as the working electrode, Platinum as the counter, and Ag/AgCl as the reference. Unlike standard self-attention mechanisms or simple concatenation fusion methods, CAFF introduces a novel dual-stream architecture that dynamically captures the inter-dependencies between raw CV signals and extracted peak data—an approach previously unexplored in electrochemical sensing. The model integrates an Improved Beluga Whale Optimization (IBWO) algorithm that automatically determines the optimal hyperparameters, resulting in a more robust model. Robustness was assessed using Chemically-Informed Degradation Simulation (CIDS). As a result, the proposed CAFF-IBWO model demonstrated superior performance, achieving R^2 values of 0.97 for Cd^{2+} and 1.00 for Pb^{2+}. It also significantly reduced the Mean Absolute Percentage Error (MAPE) by 65.79% for Cd^{2+} and 72.50% for Pb^{2+} compared to single-input attention networks. Furthermore, CAFF-IBWO exhibited remarkable resilience against signal degradation, maintaining stable prediction performance across varying noise conditions. While the study focuses specifically on Cd^{2+} and Pb^{2+} and requires further validation for broader generalization, the demonstrated performance is highly promising. These findings underscore the model's potential for real-world environmental sensing applications.

1. Introduction

The contamination of aqueous environments by heavy metals such as Cadmium (Cd^{2+}) and Lead (Pb^{2+}) poses severe threats to ecosystems and public health [1,2]. Cd^{2+} and Pb^{2+} are non-essential elements with high toxicity even at trace concentrations [3]. Cd^{2+} exposure can cause kidney failure, bone diseases, and cancer [4–6]. Meanwhile, Pb^{2+} exposure can cause permanent neurological damage, lead to cardiovascular issues, and is particularly harmful to children's developing nervous systems [7,8]. Monitoring Cd^{2+} and Pb^{2+} concentrations in water sources is therefore critical for environmental protection and public health safety.

While conventional methods like Atomic Absorption Spectroscopy (AAS) [9] and Inductively Coupled Plasma Mass Spectrometry (ICP-MS) [10,11] offer high sensitivity, their high cost and laboratory dependence limit real-time monitoring [12]. In contrast, voltammetry provides a portable, cost-effective alternative [13], though accurate quantification remains challenging due to signal complexity, overlapping peaks, and matrix effects [14].

---

* Corresponding authors.
E-mail addresses: riyanarto@its.ac.id (R. Sarno), f_taufany@chem-eng.its.ac.id (F. Taufany).

https://doi.org/10.1016/j.ceja.2026.101065
Received 6 December 2025; Received in revised form 19 January 2026; Accepted 28 January 2026

Table 1
Comparative analysis of previous studies on heavy metal estimation.

Metal detected	Method	ML/DL	Feature fusion	Hyper-parameter optimization	Model performance (R^2)	Robustness evaluation	Ref.
Cd, Cu, Pb, Ni, Zn, Cr, and Mn	AAS	–	–	–	–	–	[9]
Cd, Cu, Ni, Pb, and Zn	ICP-OES	–	–	–	–	–	[20]
Cr, Cd, Hg, and Pb	ICP-MS	–	–	–	–	–	[10]
Pb and Cd	Voltammetry	–	–	–	–	–	[21]
Cd and Cu	Voltammetry	Yes, CNN	No	No	0.996	No	[22]
Pb and Cd	Voltammetry	Yes, SVR	No	No	0.995	No	[17]
Pb and Cd	Voltammetry	Yes, Neural Network	Yes	No	Cd: 0.974 Pb: 0.999	No	[23]
Pb and Cd	Voltammetry	Yes, CAFF and CAFF-IBWO	Yes	Yes	Cd: 0.97 Pb: 1.00	Yes	This research

Machine Learning (ML) and Deep Learning (DL) have emerged as powerful tools for extracting meaningful patterns from complex data, that ideally suited for interpreting voltammetric signals [15]. The task of estimating metal concentration is fundamentally a regression problem, where the goal is to learn a mapping function from input features (the voltammetric data) to a continuous output (concentration) [16]. While traditional ML models like Support Vector Regression (SVR) have been applied [17], DL models, with their capacity for hierarchical feature learning, can automatically discover intricate relationships within the data [18]. Nevertheless, a primary challenge in developing effective regression models lies in feature representation. Raw voltammetric signals are high-dimensional and contain complex electrochemical information, making it difficult to fully capture the underlying non-linear dependencies through simple manual feature extraction methods. Current analysis often depends only on peak data [19]. However, this approach has significant limitations as it oversimplifies the data. Relying solely on peak data discards valuable signal patterns hidden in the full voltammogram, which may contain useful information that could potentially improve measurement accuracy.

Existing DL studies in voltammetry [17,22], primarily employ a comparative approach using single-input designs — relying solely on either raw voltammetric signals or extracted peak features — to determine individual efficacy rather than fusing complementary inputs. Furthermore, while data fusion has been explored [23], it typically relies on static splicing, which rigidly combines inputs without analyzing their mutual relationships. In contrast, this study introduces a collaborative Dual-Input architecture DL employing attention-based fusion, where raw voltammetric data acts as a query to dynamically weigh the importance of peak features, preventing information loss and surpassing the limitations of static concatenation.

The performance of DL models is highly dependent on their hyperparameters [24]. Manual tuning is particularly challenging because hyperparameters are often interdependent. For instance, changing the batch size typically requires a corresponding adjustment in the learning rate to maintain stability. This makes the trial-and-error process labor-intensive and prone to suboptimal results [25]. Therefore, a systematic approach to optimization becomes crucial. However, as detailed in Table 1, prior voltammetric DL studies lack comprehensive optimization strategies. Addressing this gap, this work integrates a metaheuristic-based approach for automated hyperparameter tuning.

Beyond optimization, model robustness presents a further challenge; a model may excel on pristine laboratory data yet fail when exposed to complex environmental conditions [26]. Consequently, rigorous robustness evaluation is critical. It ensures that the model remains reliable despite inevitable signal degradations and matrix variances encountered in practical deployment scenarios [27]. Table 1 shows a comparison of several previous studies that estimate heavy metals concentration, including Cd^{2+} and Pb^{2+}.

Based on the outlined background and reviewed literature, this research proposes the following contributions:

1. We propose a novel Cross-Attention Feature Fusion (CAFF) network that dynamically integrates raw voltammetric data and peak features for superior estimation accuracy of Cd^{2+} and Pb^{2+}.
2. We introduce a comprehensive robustness evaluation protocol using the Chemically-Informed Degradation Simulation (CIDS) framework to ensure model performance under realistic, non-ideal conditions.
3. We integrate the Improved Beluga Whale Optimization (IBWO) algorithm for hyperparameter tuning of the CAFF network. The performance of IBWO is compared against three other evolutionary algorithms: the Non-dominated Sorting Genetic Algorithm II (NSGA-II), Genetic Algorithm (GA), and Differential Evolution (DE).

The rest of this paper is structured as follows. Section 2 details our proposed CAFF network architecture and hyperparameter optimization approach. Section 3 presents the experimental results with discussion on model performance and robustness. Finally, Section 4 concludes the paper and suggests future research directions.

2. Proposed method

This section details the comprehensive framework developed for estimating Cd^{2+} and Pb^{2+} concentrations in aqueous samples. The methodology consist of five key stages: (1) data acquisition and preprocessing of voltammetric signals, (2) feature fusion using CAFF network, (3) hyperparameter optimization using the IBWO algorithm, (4) generation of realistic degraded data using CIDS, and (5) model robustness evaluation. Fig. 1 illustrates the integrated workflow of the proposed method.

2.1. Data acquisition and preprocessing

The experimental procedure begins with the preparation of standard solutions containing Cd^{2+} and Pb^{2+} ions. A total of 15 concentration levels were prepared for each metal, covering a range from 2 ppm to 1000 ppm. The specific concentrations used were 2, 4, 6, 8, 10, 20, 40, 60, 80, 100, 200, 400, 600, 800, and 1000 ppm. Each standard solution was formulated using high-purity $Pb(NO_3)_2$ and $Cd(NO_3)_2$ powders dissolved in a 0.1 M KCl electrolyte solution. This specific electrolyte was selected based on established studies [28,29], as it facilitates efficient electron transfer kinetics, thereby enabling the electrochemical oxidation and reduction processes of the target analytes.

Following the solution preparation, the electrochemical setup was configured using a potentiostat with a standard three-electrode system, comprising a Glassy Carbon Electrode (GCE) as the working electrode, an Ag/AgCl (with 3M KCl filling) as the reference electrode, and a Platinum wire as the counter electrode [30]. Subsequently, voltammetric measurement was conducted with specific configuration: for Cd, the potential was scanned from -1.4 V to -0.5 V, while for Pb, the scan ranged from -1.0 V to -0.1 V. The resulting current-potential data was recorded as voltammograms and saved in Excel file format, serving as the raw data for the proposed fusion model, capturing the complete

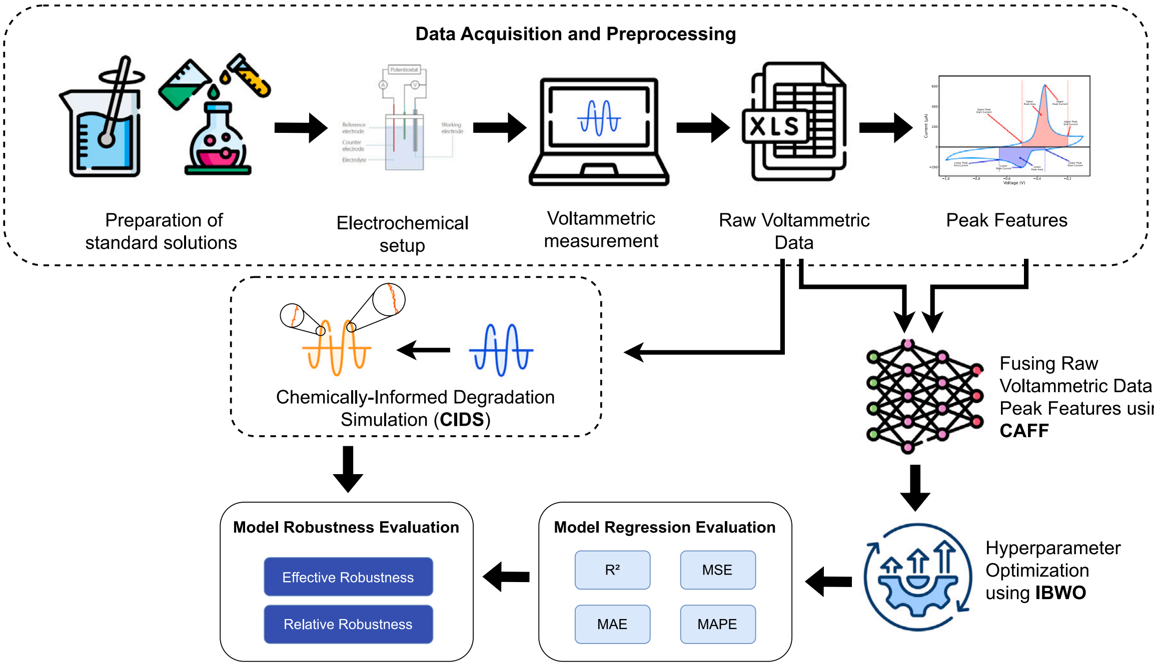

Fig. 1. The overall workflow for estimating Cd^{2+} and Pb^{2+} concentrations in water samples.

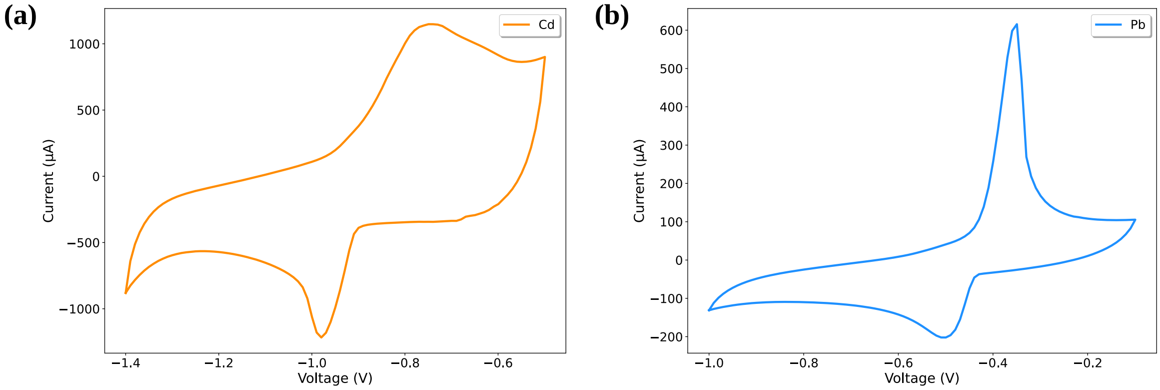

Fig. 2. Example voltammograms for (a) Cd^{2+}; and (b) Pb^{2+}.

electrochemical profile [31]. Fig. 2 displays example voltammograms for (a) Cd^{2+} and (b) Pb^{2+}, showing their characteristic upper and lower peaks. It is important to note that these distinctive peaks are not always present; at lower concentrations, the peaks can become very weak or even undetectable.

A set of 14 distinct peak features (7 for each upper and lower peak) was extracted from the voltammograms for subsequent analysis. The extracted features comprise: peak presence (a binary Yes/No indicator), start current of the peak, peak current, end current of the peak, peak area, skewness of the peak, and kurtosis of the peak.

The peak feature extraction process utilizes an automated signal processing algorithm based on Topographic Prominence. This metric measures the vertical distance between a peak's apex and its lowest surrounding contour line, quantifying how much a peak stands out relative to the local baseline. Accordingly, the peak current is determined as the local maximum value at the identified apex. When a peak is successfully detected using this criterion, the integration boundaries are determined dynamically based on the peak's geometry (specifically the Width at Relative Height). Conceptually, this method identifies the peak's apex and projects downwards to the base of the signal. The specific points where the horizontal width line at this level intersects the left and right slopes of the peak are identified as the start current and end current of the peak.

Consequently, the peak area is defined by the region between the start current and end current points, as illustrated in Fig. 3. The peak area is calculated using a discrete summation approach. This method partitions the region under the curve into multiple narrow rectangles, each with a fixed potential interval (ΔE) and a height equal to the measured current (I) at that specific potential (E). The total area is then obtained by summing the areas of all these individual rectangles, following the formulation in Eq. (1).

$$\text{Area} = \sum_{i=1}^{n} f(x_i) \cdot \Delta x \tag{1}$$

Where $f(x_i)$ is the function value (current) at point x_i, n is the total number of discrete points (or intervals) within the range of the peak, and Δx is the difference between two adjacent potential values.

In cases where a distinct peak is absent from the voltammogram, such as in low-concentration samples where signal detection is challenging, the area is calculated within a predefined fix potential window to ensure consistent feature extraction. The specific voltage ranges applied are (−0.9 V, −0.6 V) for the upper window and (−1.1 V, −0.8 V) for the lower window of Cd. For Pb, the upper window is defined as (−0.4 V, −0.2 V) and the lower window as (−0.6 V, −0.4 V). These potential windows were empirically determined based on

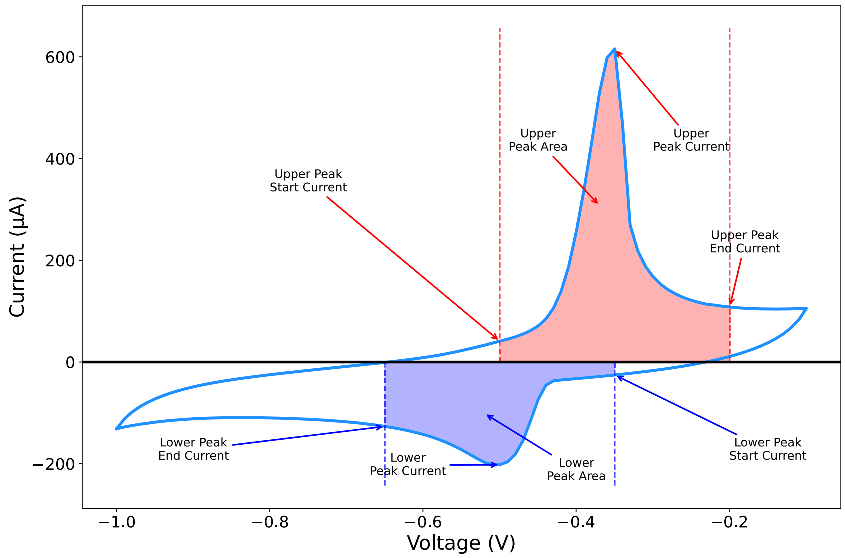

Fig. 3. Illustration of upper and lower peak area.

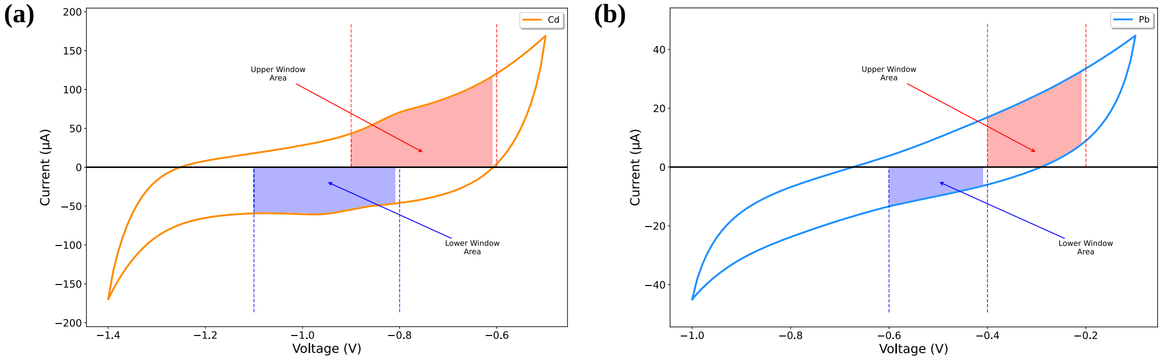

Fig. 4. Illustration of the fixed-window area calculation method applied to voltammograms without distinct peaks for (a) Cd^{2+}; and (b) Pb^{2+}.

the peak locations observed in high-concentration voltammograms, ensuring that the integration captures the region of interest where the electrochemical reaction occurs. This fixed-window area calculation approach is illustrated in Fig. 4 for (a) Cd^{2+} and (b) Pb^{2+}. Furthermore, skewness and kurtosis are computed to quantify the peak's shape. Skewness measures the asymmetry of the current distribution around the peak [32], while kurtosis indicates its sharpness [33].

2.2. CAFF network architecture for fusing raw signals and peak features

Cross-Attention Feature Fusion (CAFF) network is designed to integrate two complementary types of voltammetric features to enhance model performance in estimating the concentrations of heavy metals Cd^{2+} and Pb^{2+}. The two input features are the raw voltammetric data and the extracted peak feature from the previous stage. By applying cross-attention between these two feature sets, the model can dynamically identify and combine the most informative aspects of both representations, producing a more robust and context-enriched feature embedding. Fig. 5 shows the proposed CAFF network architecture.

In CAFF, the raw voltammetric data act as the query channel (Q), while the extracted signal shape features serve as the key channel (K) and value channel (V). The input representations are defined in Eq. (2).

$$\text{Input} \quad \begin{cases} I \in \mathbb{R}^{L_I \times d} \\ p \in \mathbb{R}^{L_p \times d} \end{cases} \tag{2}$$

Where I is the current in raw voltammetric data, p is the peak features, L_I is the number of current values in the raw voltammetric data, L_p is the number of peak features, and d is the embedding dimension.

Each input is first transformed through a linear projection layer to a shared embedding dimension (d). Learnable positional encodings are added to encode the sequential order of the voltammetric scan, which is crucial for preserving electrochemical information tied to applied potential. The resulting representations then serve as the query, key, and value matrices, as formulated in Eq. (3).

$$Q = IW_Q, \quad K = pW_K, \quad V = pW_V \tag{3}$$

Where Q, K, V denote the query, key, and value matrices, respectively. W_Q, W_K, and W_V denote the corresponding learnable projection weights for each mapping.

The attention mechanism computes the similarity between the query (Q) and key (K) matrices through Eq. (4) [34].

$$A = \text{softmax}\left(\frac{QK^T}{\sqrt{d}}\right) \tag{4}$$

Where A represents the attention score matrix, and K^T is the transpose of K. This operation allows each element in the raw voltammetric data to selectively attend to the most relevant regions of the extracted peak features. The attention score is then applied to the value (V) matrix to generate the cross-attention output as defined in Eq. (5).

$$a' = A \bullet V \tag{5}$$

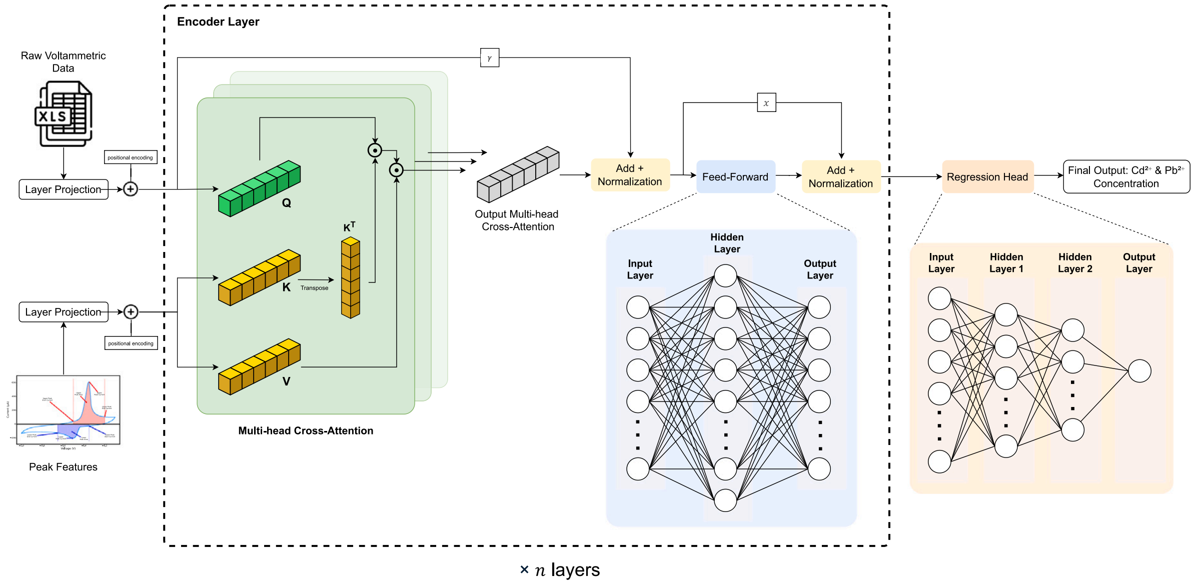

Fig. 5. The proposed CAFF network architecture for estimating Cd^{2+} and Pb^{2+} concentrations from fused raw voltammetric data and peak features.

Table 2
Hyperparameter search space for the CAFF model optimization.

Hyperparameter	Symbol	Description	Search values	Ref.
Model dimension	d_model	Size of the feature vector representation at each model layer.	{64, 128, 256}	[35–37]
Attention heads	nhead	Number of parallel attention mechanisms within each encoder layer.	{4, 8, 16}	[36,38,39]
Encoder layers	num_layers	Total count of stacked encoder blocks in the architecture.	{2, 3, 4}	[36,37,40]
Dropout rate	dropout	Fraction of neurons randomly deactivated to prevent overfitting.	{0.1, 0.2, 0.3}	[37,41,42]
Learning rate	lr	Step size magnitude controlling weight updates during optimization.	{0.0005, 0.001, 0.002}	[43–45]

Where a' is the Multi-head Cross-Attention result that captures information from both raw voltammetric data and peak features. Subsequently, a' is combined with the residual (γ) from the first stage and normalized using LayerNorm according to Eq. (6).

$$x = \mathrm{LayerNorm}(a' + \gamma) \tag{6}$$

Where x is the normalized matrix. This matrix (x) then passes through a Feed-Forward layer using Eq. (7).

$$h = \sigma\left(xW_1 + b_1\right)W_2 + b_2 \tag{7}$$

Here, h represents the feature fusion result matrix, σ is the activation function, x is the Feed-Forward layer input originating from the normalized matrix. W_1, W_2 and b_1, b_2 are the weights and biases of the two linear layers, respectively.

A second residual connection combines h with x, followed by another LayerNorm, producing the output of encoder layer. This encoder layer can be repeated multiple (n) times before the final representation is passed to a regression head, generating the estimated Cd^{2+} and Pb^{2+} concentrations.

The performance of the proposed CAFF model is rigorously compared against a standard attention network, commonly known as a Transformer Encoder (TE) [46]. Two TE variants are examined: a model using only peak features (TE-Peak) and a model using only raw voltammetric data (TE-Raw). This comparison is particularly meaningful because both CAFF and TE share the same fundamental attention mechanism, enabling a direct evaluation of the CAFF's architectural enhancements. Model performance is evaluated using R^2, MSE, MAE, and MAPE [47] under stratified 5-fold cross-validation [48]. Results are presented as boxplots displaying average metric values and standard deviations to highlight stability. Additionally, training-validation loss curves are analyzed to verify generalization and ensure the absence of overfitting [49].

2.3. Hyperparameter tuning using IBWO

The optimization of the CAFF model is conducted using the IBWO algorithm for hyperparameter tuning. IBWO is an enhanced metaheuristic algorithm that addresses limitations in the standard BWO approach through two significant enhancements [50]. First, chaotic map initialization using logistic chaotic mapping enhances population diversity in IBWO. This initialization strategy promotes a more uniform distribution of initial solutions across the search space, thereby preventing premature convergence to local optima. The mathematical representation of this chaotic mapping is provided in Eq. (8).

$$x_{a+1} = 4x_a(1 - x_a) \tag{8}$$

Where x_a and x_{a+1} represent chaotic values between 0 and 1 at iterations a and $a+1$, respectively.

Second, a non-linear exploration probability mechanism is implemented in IBWO. This adaptive approach facilitates extensive global exploration during initial iterations, with a progressive shift toward intensive local exploitation in later stages. Consequently, the balance between exploration and exploitation is effectively maintained throughout the optimization process. The formulation of this mechanism is defined in Eq. (9).

$$p(T) = 1 - \frac{T}{T_{\max}} \tag{9}$$

Where $p(T)$ denotes the exploration probability at iteration T and $T_{\max}$ represents the maximum number of iterations.

The hyperparameter optimization process for the CAFF network architecture focuses on five key parameters, as detailed in Table 2. These search intervals were established based on a synthesis of optimal ranges reported in prior deep learning studies. This approach allows the optimization algorithm to focus directly on the most promising parameter

Table 3

Internal settings for the applied optimization algorithms.

Algorithm	Parameter	Value/Setting
IBWO	Balance factor	0.5
	Levy flight parameter	1.5
	Chaotic map function	Logistic map (Eq. (8))
GA	Crossover rate	0.8
	Mutation rate	0.1
	Selection strategy	Tournament selection
NSGA-II	Selection strategy	Binary tournament
	Mutation rate	0.1
	Sorting strategy	Non-Dominated sorting
	Diversity strategy	Crowding distance
	Crossover rate	0.9
DE	Scaling factor	0.8
	Crossover rate	0.7

regions, thereby improving search efficiency and avoiding unnecessary exploration of improbable values. The optimization utilizes MSE as the fitness function to identify hyperparameter configurations that minimize prediction errors.

The performance evaluation of IBWO includes comparisons with three established evolutionary algorithms: GA [51,52], NSGA-II [53,54], and DE [55,56]. These methods were selected based on their foundation in natural-inspired optimization principles. To ensure a rigorous and consistent evaluation, the hyperparameter optimization process utilized the same stratified 5-fold cross-validation framework described in Section 2.2. Most importantly, the exact same data folds were applied across all evaluated algorithms (IBWO, GA, NSGA-II, and DE) to avoid any bias from data splitting. Furthermore, to ensure reproducibility, the specific internal parameter settings for all applied algorithms are provided in Table 3.

Regarding the proposed IBWO, the balance factor and Levy flight index were set to 0.5 and 1.5, respectively, following recommendations of the standard literature [57]. For the computational budget, a standardized configuration was applied across all algorithms, where the population size and maximum iterations were both set to 10. This specific configuration was adopted primarily due to the high computational cost of the fitness function, which involves training a deep learning model under a 5-fold cross-validation scheme. Crucially, the limited population size is effectively compensated by the IBWO's chaotic initialization mechanism using the Logistic Map (Eq. (8)). Unlike standard random initialization, the Logistic Map ensures a highly uniform distribution of the initial population across the search space, thereby maximizing exploration diversity even with fewer agents. Furthermore, the selection of these specific constraints is supported by prior studies [58], which demonstrated that metaheuristic optimization — specifically the IBWO algorithm — utilizing a population size of 10 and 10 iterations can still yield significant improvements in deep learning model performance.

2.4. Chemically-informed degradation simulation (CIDS)

To evaluate model robustness under realistic electrochemical sensor conditions, a CIDS framework is developed. This module generates degraded voltammetric data by simulating five common sensor degradation phenomena that occur in real-world measurements: baseline drift, random electronic noise, peak broadening, signal attenuation, and low-frequency thermal drift. A degradation level of 0.03 was set to represent moderate sensor deterioration. The output consists of degraded voltammograms that retain the original voltage–current relationship while displaying distortion patterns characteristic of aged electrochemical sensors.

2.5. Model robustness evaluation

Model robustness is assessed using two metrics: Effective Robustness (ρ) to gauge stability under shifts, and Relative Robustness (τ) to quantify the impact of interventions [59]. In this study, ρ and τ are derived using MSE to reflect prediction consistency under degraded conditions. The metrics are calculated based on four specific values: $\mathrm{MSE}_1(f)$ and $\mathrm{MSE}_2(f)$ represent the performance of the proposed model f on the standard and degraded test sets, respectively, while $\mathrm{MSE}_1(f_{\mathrm{base}})$ and $\mathrm{MSE}_2(f_{\mathrm{base}})$ denote the corresponding performance for the baseline model f_{base}.

The effective robustness is defined by Eq. (10):

$$\rho = \mathrm{MSE}_2(f) - \beta(\mathrm{MSE}_1(f)) \tag{10}$$

Where $\beta(x)$ denotes the expected baseline MSE on degraded test set for given MSE on standard test set, derived from log-linear fitting of baseline models.

The relative robustness is defined by Eq. (11):

$$\tau = \mathrm{MSE}_2(f) - \mathrm{MSE}_2(f_{\mathrm{base}}) \tag{11}$$

Robustness is demonstrated by negative values for both metrics, where lower (more negative) values indicate higher degree of robustness against data degradation.

3. Results and discussions

3.1. Data characteristics and preprocessing results

This study utilizes a voltammetric dataset of 1500 voltammograms, comprising 750 measurements each for Cd^{2+} and Pb^{2+}. Each metal is represented by 15 concentration levels, with 50 samples per level.

Fig. 6 presents the voltammetric profiles for both Cd^{2+} and Pb^{2+}. Figs. 6a (Cd^{2+}) and 6b (Pb^{2+}) provide 3D visualizations, plotting a single representative voltammogram per concentration level. Furthermore, to accommodate the wide dynamic range of the response and prevent the smaller peaks at low concentrations from being obscured by the larger signals, the 2D visualizations are separated into distinct concentration ranges. Figs. 6c and 6d display the profiles for the 200–1000 ppm concentration range, while Figs. 6e and 6f detail the 2–100 ppm concentration range for Cd^{2+} and Pb^{2+}, respectively. A key observation is the strong concentration dependence of peak prominence - at lower concentrations, the peaks become significantly weaker and broader. This phenomenon poses a substantial challenge for accurate quantification, which the proposed CAFF network specifically aims to address through its dual-pathway feature fusion approach.

3.2. Performance analysis of CAFF-IBWO model

This section evaluates the performance of CAFF-IBWO in estimating Cd^{2+} and Pb^{2+} concentrations. The analysis begins with a comparison against single-feature TE baselines, followed by an examination of hyperparameter optimization methods (including IBWO), predictive performance visualization, and overfitting analysis.

3.2.1. CAFF performance

The CAFF model was evaluated against single-modality baselines (TE-Peak and TE-Raw), with results detailed in Table 4. The result reveals a clear hierarchy: models utilizing raw signals (TE-Raw and CAFF) substantially outperform the peak-only approach (TE-Peak), which exhibited high error rates (MAPE > 100%). This confirms that critical information is embedded within the complete signal structure beyond just peak parameters. Most importantly, CAFF outperforms the best single-stream baseline (TE-Raw), achieving a 6%–9% reduction in MSE and MAE for both metals. This improvement validates the cross-attention mechanism, which effectively contextualizes raw signals with peak metrics.

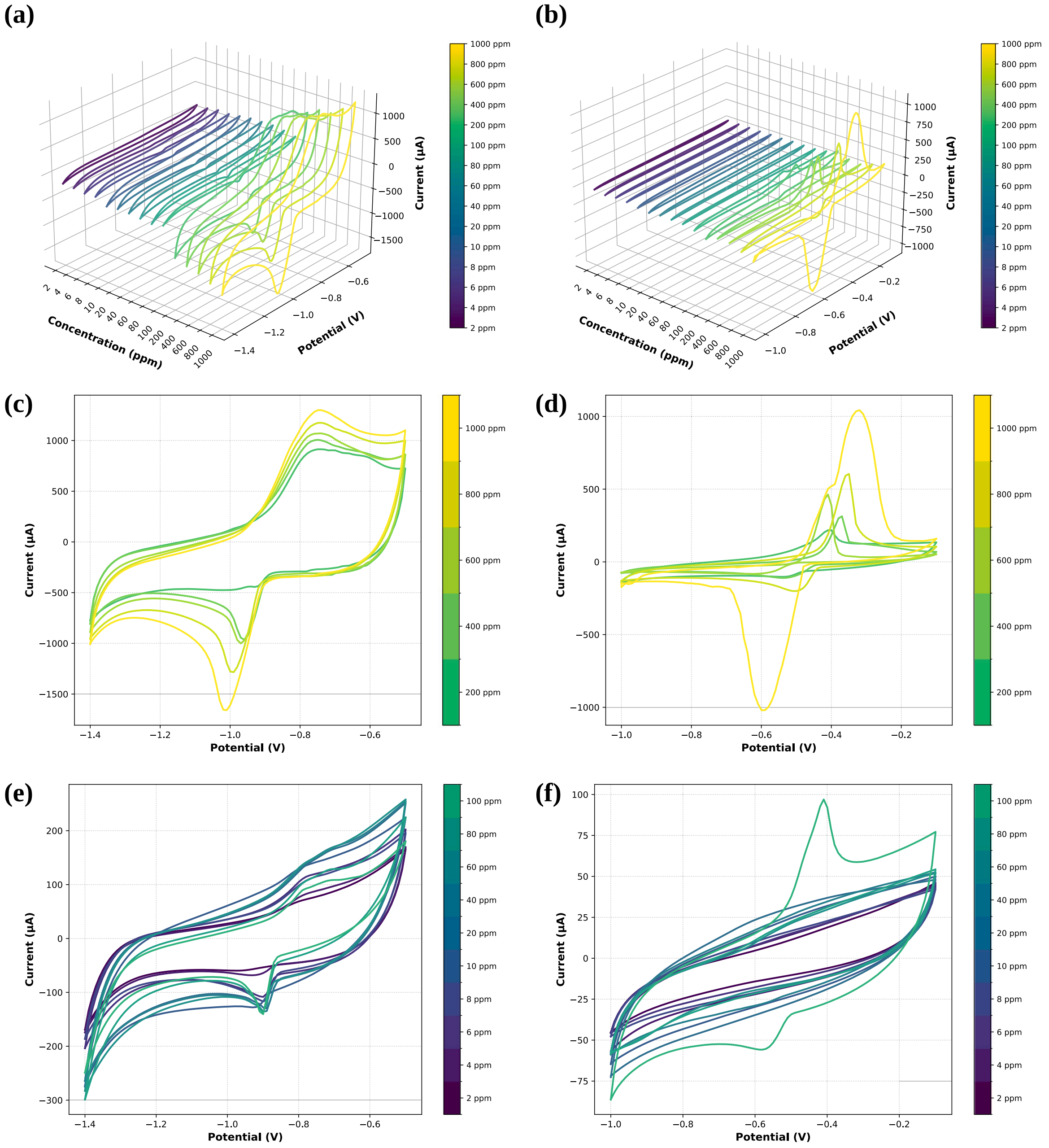

Fig. 6. Voltammetric profiles of Cd^{2+} (a, c, e) and Pb^{2+} (b, d, f). (a–b) 3D representations, with corresponding 2D plots for (c–d) 200–1000 ppm and (e–f) 2–100 ppm ranges.

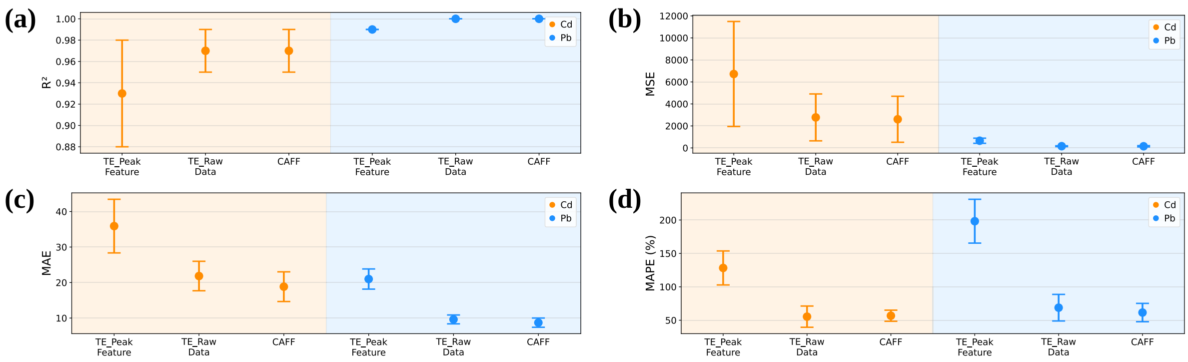

Fig. 7. Performance distribution of the TE-Peak, TE-Raw, and CAFF models across validation folds for (a) R^2; (b) MSE; (c) MAE; and (d) MAPE metrics. The boxplots visualize the mean (central point) and variability (standard deviation range) of each model's performance.

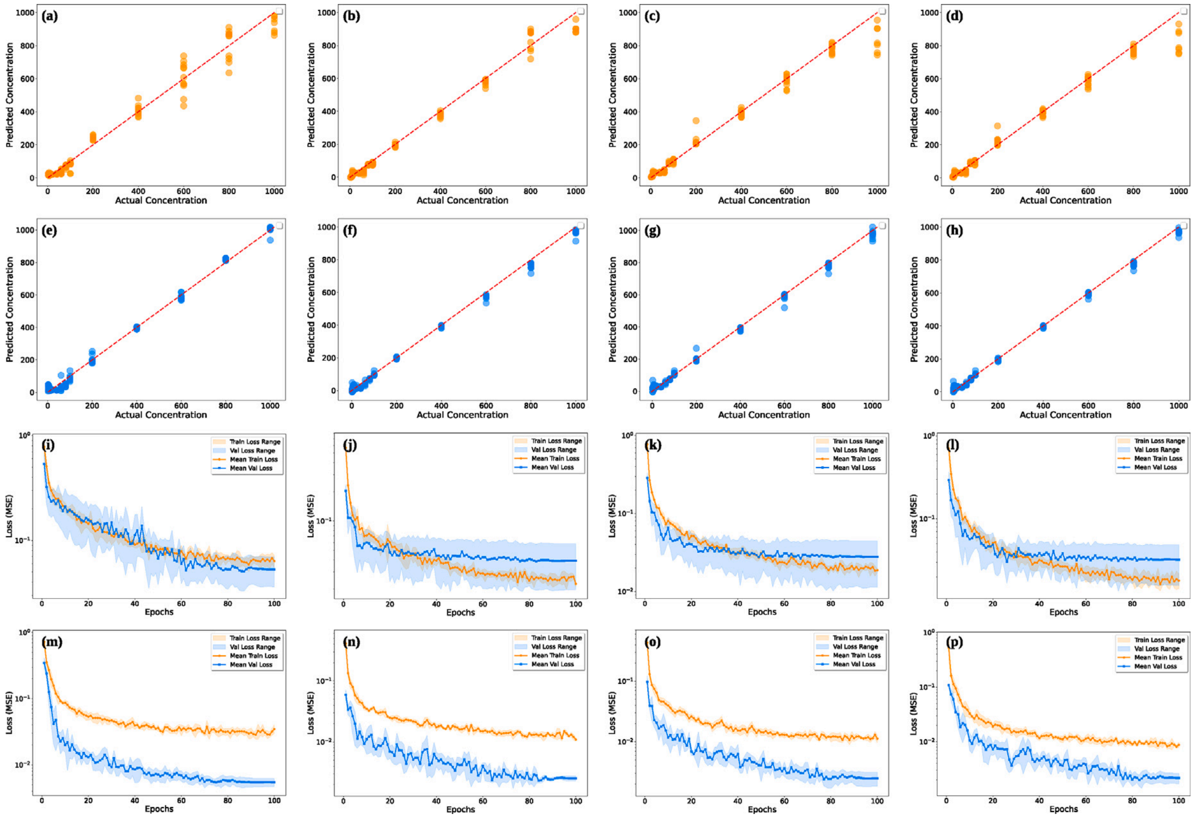

Fig. 8. Comprehensive visualization of model performance and training dynamics for Cd^{2+} (a–d, i–l) and Pb^{2+} (e–h, m–p) estimation. (a–d, e–h) Prediction versus actual concentration plots for (a, e) TE-Peak; (b, f) TE-Raw; (c, g) CAFF; and (d, h) CAFF-IBWO models. (i–p) Corresponding training and validation loss curves, demonstrating convergence behavior and generalization capability across epochs.

Table 4
Performance comparison of CAFF against Transformer Encoder (TE) models using single data types (raw data only or peak features only) for Cd^{2+} and Pb^{2+} concentration estimation.

Heavy metal category	Model	Metric			
		R^2	MSE	MAE	MAPE
Cd^{2+}	TE-Peak	0.93	6718.03	35.90	128.27
	TE-Raw	0.97	2774.28	21.84	55.36
	CAFF	**0.97**	**2605.67**	**18.84**	**56.76**
Pb^{2+}	TE-Peak	0.99	654.35	20.99	198.25
	TE-Raw	0.99	158.39	9.62	68.78
	CAFF	**0.99**	**151.55**	**8.71**	**61.49**

Notably, in Fig. 7, CAFF exhibits the smallest standard deviation across all evaluation metrics for both metals, indicating its superior stability and consistent generalization capability across all data folds. Visual analysis of prediction plots (Figs. 8a – 8c and 8e – 8g) confirms that CAFF achieves the tightest clustering along the ideal regression line, while all loss curves (Figs. 8i – 8k and 8m – 8o) demonstrate stable convergence without overfitting.

3.2.2. Hyperparameter optimization results

The impact of hyperparameter tuning was assessed by comparing IBWO against GA, NSGA-II, DE, and the untuned CAFF baseline (Table 5). To ensure a fair and rigorous comparison, all evaluated optimization algorithms were executed using the identical search space and parameter constraints as defined previously in Table 2. The results indicate that standard metaheuristics (GA, NSGA-II, DE) occasionally yielded suboptimal configurations, leading to higher error rates than the baseline. In contrast, CAFF-IBWO consistently delivered the best performance. It maintained high R^2 scores while significantly reducing MAPE by 22.7% for Cd^{2+} and 11.3% for Pb^{2+} compared to the baseline, confirming that the optimized hyperparameters effectively refine the model's precision.

Table 5
Performance comparison of CAFF optimized with different hyperparameter tuning algorithms.

Heavy metal category	Model	Metric			
		R^2	MSE	MAE	MAPE
Cd^{2+}	CAFF	0.97	2605.67	18.84	56.76
	CAFF-IBWO	**0.97**	**2585.47**	**18.70**	**43.88**
	CAFF-NSGAII	0.97	2694.95	19.47	50.01
	CAFF-GA	0.97	2596.47	19.18	47.14
	CAFF-DE	0.97	2611.45	19.01	56.94
Pb^{2+}	CAFF	1.00	151.55	8.71	61.49
	CAFF-IBWO	**1.00**	**148.58**	**7.45**	**54.53**
	CAFF-NSGAII	1.00	170.23	8.56	61.34
	CAFF-GA	1.00	167.68	8.37	58.89
	CAFF-DE	1.00	128.70	7.19	60.35

Furthermore, visual analysis confirms the superior performance of the IBWO-tuned model. The predictive plots in Figs. 8d and 8h show the tightest clustering along the regression line, while boxplot analysis (Fig. 9) reveals that CAFF-IBWO exhibits the lowest standard deviation across folds, indicating superior consistency in its performance. These advantages are attributed to IBWO's chaotic initialization and adaptive exploration mechanism, which navigates the complex hyperparameter

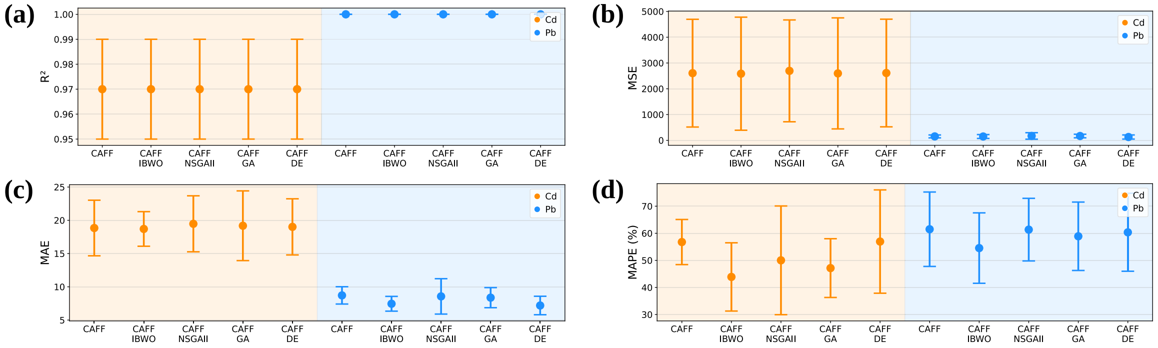

Fig. 9. Performance evaluation of the CAFF models across validation folds for (a) R^2; (b) MSE; (c) MAE; and (d) MAPE metrics. The boxplots visualize the mean (central point) and variability (standard deviation range) of each model's performance.

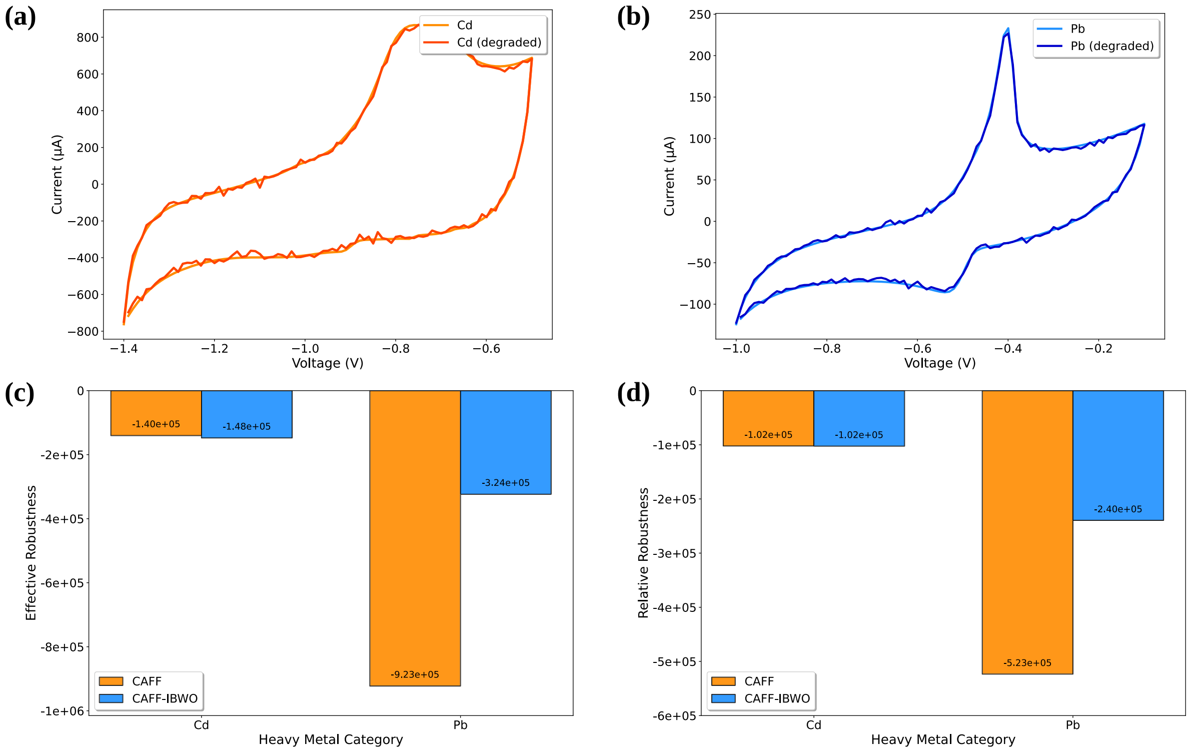

Fig. 10. Signal degradation and robustness analysis. (a–b) Original vs. CIDS-degraded voltammograms for (a) Cd^{2+} and (b) Pb^{2+}; (c–d) Effective (ρ) and Relative (τ) robustness comparison between CAFF and CAFF-IBWO models on degraded data.

space more effectively than other algorithms. Finally, the learning curves (Figs. 8l, 8p) display minimal validation gaps, especially in the Pb^{2+} learning curve, demonstrating that CAFF-IBWO achieves robust generalization with a markedly lower risk of overfitting compared to other configurations.

3.3. Robustness evaluation using CIDS-generated data

The model's resilience against sensor degradation was assessed using 150 CIDS-generated samples per metal. Figs. 10a and 10b illustrate representative 200 ppm voltammograms for (a) Cd^{2+} and (b) Pb^{2+} after CIDS degradation, showing significant noise and baseline fluctuations compared to the original signals. Figs. 10c and 10d compares the ρ and τ metrics. The results demonstrate that both CAFF and CAFF-IBWO exhibit strong robustness characteristics, with each model showing particular suitability for different metal species.

For Cd^{2+} estimation, CAFF-IBWO demonstrates excellent robustness properties, with ρ and τ values of −147,750 and −102,466, respectively. The standard CAFF also maintains good robustness with values of −140,393 and −102,188, confirming that both architectures provide reliable performance for Cd^{2+} detection under data degradation conditions. In Pb^{2+} estimation, the standard CAFF shows remarkable robustness with ρ value of −922,714 and τ value of −523,440. CAFF-IBWO also maintains substantial robustness with values of −323,652 and −239,561, respectively, indicating that both models are well-suited for Pb^{2+} estimation. The differential performance patterns reveal complementary advantages between the two approaches, with each model demonstrating robust characteristics for specific metal types. CAFF-IBWO shows excellent adaptation for Cd^{2+} detection, potentially due to its optimized handling of complex voltammetric signals, while the standard CAFF exhibits strong inherent suitability for Pb^{2+} estimation. Importantly, both CAFF and CAFF-IBWO significantly outperformed the

TE-Peak feature baseline across all robustness metrics, collectively confirming the advantage of cross-attention feature fusion in maintaining stable performance under data degradation conditions for Cd^{2+} and Pb^{2+} estimation.

4. Conclusions

This study presents a robust framework for detecting Cd^{2+} and Pb^{2+} in water samples by integrating raw voltammetric data and peak features through cross-attention fusion enhanced with evolutionary optimization. The proposed CAFF-IBWO model demonstrates superior estimation accuracy with R^2 values of 0.97 for Cd^{2+} and 1.00 for Pb^{2+}. Compared to the standard CAFF model without optimization, it achieves a significant MAPE reduction of 11%–23%. Furthermore, when evaluated against the standard attention network with a single feature (TE-Peak), the CAFF-IBWO model shows a remarkable improvement, reducing the MAPE by 65.79% for Cd^{2+} and 72.50% for Pb^{2+} estimation. The robustness evaluation under data degradation confirms that both CAFF and CAFF-IBWO maintain reliable performance in estimating Cd^{2+} and Pb^{2+} concentrations. This framework provides a reliable solution for environmental monitoring that remains accurate even with suboptimal data quality, with future work focusing on validation with diverse real-world samples.

CRediT authorship contribution statement

Rizqy Ahsana Putri: Writing – original draft, Validation, Methodology, Formal analysis, Conceptualization. **Riyanarto Sarno:** Writing – review & editing, Supervision, Investigation. **Wahyu Prasetyo Utomo:** Visualization, Software, Formal analysis. **Fadlilatul Taufany:** Writing – review & editing, Validation, Methodology. **Kelly Rossa Sungkono:** Resources, Project administration, Funding acquisition. **Taufiq Choirul Amri:** Visualization, Investigation. **Alya Kamilah:** Investigation, Data curation. **Rini Handayani:** Investigation, Data curation. **Sang-Seok Lee:** Writing – review & editing, Supervision. **A. Min Tjoa:** Writing – review & editing, Validation. **Arif Abdullah Sagran:** Visualization, Validation.

Declaration of competing interest

The authors declare that they have no known competing financial interests or personal relationships that could have appeared to influence the work reported in this paper.

Acknowledgments

This work was funded by the Indonesian Endowment Fund for Education (LPDP) on behalf of the Indonesian Ministry of Higher Education, Science and Technology and managed under the EQUITY Program (Contract No. 4299/B3/DT.03.08/2025 & No 3029/PKS/ITS/2025); the Directorate General of Higher Education, Research, and Technology of the Republic of Indonesia under Penelitian Pendidikan Magister menuju Doktor untuk Sarjana Unggul (PMDSU) (Contract No. 017/C3/DT.05.00/PL/2025 and No. 1179/PKS/ITS/2025); the ITS under Program Riset Penugasan ITS Strategic Research Grant (SRG); National Research and Innovation Agency (BRIN) under RIIM Kompetisi Gelombang 10 Program; HETI ADB ITS under Penelitian Post-Doctoral; and the Indonesian Ministry of Higher Education, Science and Technology under Skema SINERGI Hilirisasi Inovasi Komersial.

Data availability

Data will be made available on request.

References

[1] W. Xu, Y. Jin, G. Zeng, Introduction of heavy metals contamination in the water and soil: a review on source, toxicity and remediation methods, Green Chem. Lett. Rev. 17 (1) (2024) http://dx.doi.org/10.1080/17518253.2024.2404235.

[2] Q. Zhou, N. Yang, Y. Li, B. Ren, X. Ding, H. Bian, X. Yao, Total concentrations and sources of heavy metal pollution in global river and lake water bodies from 1972 to 2017, Glob. Ecol. Conserv. 22 (2020) e00925, http://dx.doi.org/10.1016/j.gecco.2020.e00925.

[3] G.A. Francis, S.S. Jeyakumar, S. Ray, S. Supreethee, R. Vashishth, Emerging roles of FTIR spectroscopy in toxic metal profiling: innovations for food safety monitoring, Food Saf. Risk 12 (2025) 9, http://dx.doi.org/10.1186/s40550-025-00119-9.

[4] Y. Lei, M. Guo, J. Xie, X. Liu, X. Li, H. Wang, Y. Xu, D. Zheng, Relationship between blood cadmium levels and bone mineral density in adults: a cross-sectional study, Front. Endocrinol. 15 (2024) http://dx.doi.org/10.3389/fendo.2024.1354577.

[5] P. Rasin, A.A. V, S.M. Basheer, J. Haribabu, J.F. Santibanez, C.A. Garrote, A. Arulraj, R.V. Mangalaraja, Exposure to cadmium and its impacts on human health: A short review, J. Hazard. Mater. Adv. 17 (2025) 100608, http://dx.doi.org/10.1016/j.hazadv.2025.100608.

[6] C.T. Kunioka, J.C. Cruz, V.C. de Oliveira Souza, B.A. Rocha, F. Barbosa, L. Belo, M.C. Manso, M. Carvalho, Low-level environmental cadmium exposure and its effects on renal and bone health in Brazilian postmenopausal women: A cross-sectional study, Expo. Health 17 (2025) 1131–1145, http://dx.doi.org/10.1007/s12403-025-00715-2.

[7] M.S. Collin, S.K. Venkatraman, N. Vijayakumar, V. Kanimozhi, S.M. Arbaaz, R.G.S. Stacey, J. Anusha, R. Choudhary, V. Lvov, G.I. Tovar, F. Senatov, S. Koppala, S. Swamiappan, Bioaccumulation of lead (Pb) and its effects on human: A review, J. Hazard. Mater. Adv. 7 (2022) 100094, http://dx.doi.org/10.1016/j.hazadv.2022.100094.

[8] J. Li, M. Hu, Y. Liu, R. Lu, W. Feng, Lead exposure leads to premature neural differentiation via inhibiting Wnt signaling, Environ. Pollut. 363 (2024) 125232, http://dx.doi.org/10.1016/j.envpol.2024.125232.

[9] S. Anwar, Q.A. Syed, A. Ullah, M. Arshad, S.N. Khan, M.I. Hussain, Detection of heavy metals using atomic absorption and emission spectroscopy in drinking water of Faisalabad, Pakistan: microbial safety and quality status assessment, Toxin Rev. 43 (2024) 1–17, http://dx.doi.org/10.1080/15569543.2023.2272174.

[10] Y. Song, F. Guo, P. Zeng, J. Liu, Y. Wang, H. Cheng, Simultaneous measurements of Cr, Cd, Hg and Pb species in ng L^{-1} levels by interfacing high performance liquid chromatography and inductively coupled plasma mass spectrometry, Anal. Chim. Acta 1212 (2022) 339935, http://dx.doi.org/10.1016/j.aca.2022.339935.

[11] I.A. Alhagri, A.N. Al-Hakimi, S.M. Al-Hazmy, A.E. Albadri, Determination of trace and heavy metals in bottled drinking water in Yemen by ICP-MS, Results Chem. 8 (2024) 101558, http://dx.doi.org/10.1016/j.rechem.2024.101558.

[12] S.A. Lahari, N. Kumawat, K. Amreen, R.N. Ponnalagu, S. Goel, IoT integrated and deep learning assisted electrochemical sensor for multiplexed heavy metal sensing in water samples, Npj Clean Water 8 (2025) 10, http://dx.doi.org/10.1038/s41545-025-00441-x.

[13] P.L. Kyabutwa, N. Alyamni, J.L. Abot, A.G. Zestos, Recent trends in electrochemical methods for real-time detection of heavy metals in water and soil: A review, Curr. Opin. Electrochem. 54 (2025) 101749, http://dx.doi.org/10.1016/j.coelec.2025.101749.

[14] J. Liu, J. Li, Y. Xu, S.S. Low, H. Ning, S. Yu, D. Xu, Q. Liu, A fused convolutional transformer for voltammetric electronic tongue analysis tasks, J. Environ. Chem. Eng. 12 (2024) 113462, http://dx.doi.org/10.1016/j.jece.2024.113462.

[15] J.X. Leon-Medina, D.A. Tibaduiza, J.C. Burgos, M. Cuenca, D. Vasquez, Classification of As, Pb and Cd heavy metal ions using square wave voltammetry, dimensionality reduction and machine learning, IEEE Access 10 (2022) 7684–7694, http://dx.doi.org/10.1109/ACCESS.2022.3143451.

[16] T.-M. Dutschmann, V. Schlenker, K. Baumann, Chemoinformatic regression methods and their applicability domain, Mol. Inform. 43 (2024) http://dx.doi.org/10.1002/minf.202400018.

[17] N. Liu, G. Zhao, G. Liu, Accurate SWASV detection of Cd(II) under the interference of Pb(II) by coupling support vector regression and feature stripping currents, J. Electroanal. Chem. 889 (2021) 115227, http://dx.doi.org/10.1016/j.jelechem.2021.115227.

[18] W. Zhi, A.P. Appling, H.E. Golden, J. Podgorski, L. Li, Deep learning for water quality, Nat. Water 2 (2024) 228–241, http://dx.doi.org/10.1038/s44221-024-00202-z.

[19] N. Liu, W. Ye, G. Zhao, G. Liu, Development of smartphone-controlled and machine-learning-powered integrated equipment for automated detection of bioavailable heavy metals in soils, J. Hazard. Mater. 465 (2024) 133140, http://dx.doi.org/10.1016/j.jhazmat.2023.133140.

[20] Y. Wu, X. Gao, Y. Li, Application of inductively coupled plasma optical emission spectrometer in water quality monitoring, Desalination Water Treat. 314 (2023) 314–321, http://dx.doi.org/10.5004/dwt.2023.30036.

[21] S. Perveen, J.A. Baig, S.T.H. Sherazi, H.I. Afridi, E. Fricovsky, S. Sanam, K. Akhtar, Graphene oxide/magnesium ferrite nanocomposite modified electrochemical sensor for simultaneous detection of cadmium and lead, Microchem. J. 214 (2025) 114148, http://dx.doi.org/10.1016/j.microc.2025.114148.

[22] Z.-W. Gao, Y. Yu, S.-H. Chen, Y.-Y. Li, Z.-H. Liu, M. Yang, P.-H. Li, Z.-Y. Song, X.-J. Huang, Machine learning-driven simultaneous quantification of Cd(II) and Cu(II) on Co2P/CoP heterostructure: enhanced electrochemical signals via activated Co-P electron bridge, J. Hazard. Mater. 491 (2025) 138030, http://dx.doi.org/10.1016/j.jhazmat.2025.138030.

[23] X. Wang, W. Lin, C. Chen, L. Kong, Z. Huang, D. Kirsanov, A. Legin, H. Wan, P. Wang, Neural networks based fluorescence and electrochemistry dual-modal sensor for sensitive and precise detection of cadmium and lead simultaneously, Sensors Actuators B: Chem. 366 (2022) 131922, http://dx.doi.org/10.1016/j.snb.2022.131922.

[24] S. Hanifi, A. Cammarono, H. Zare-Behtash, Advanced hyperparameter optimization of deep learning models for wind power prediction, Renew. Energy 221 (2024) 119700, http://dx.doi.org/10.1016/j.renene.2023.119700.

[25] A.A. Ali, M.T. Hammad, H.S. Hassan, A co-evolutionary genetic algorithm approach to optimizing deep learning for brain tumor classification, IEEE Access 13 (2025) 21229–21248, http://dx.doi.org/10.1109/ACCESS.2025.3535844.

[26] M. Jeferson, et al., Road surface type classification based on inertial sensors and machine learning, Comput. Arch. Inform. Numer. Comput. 103 (10) (2021) 2143–2170, http://dx.doi.org/10.1007/s00607-021-00914-0.

[27] A. Arsenos, V. Karampinis, E. Petrongonas, C. Skliros, D. Kollias, S. Kollias, A. Voulodimos, Common corruptions for evaluating and enhancing robustness in air-to-air visual object detection, IEEE Robot. Autom. Lett. 9 (7) (2024) 6688–6695, http://dx.doi.org/10.1109/LRA.2024.3408485.

[28] S. Ghrkhlari, F. Ahour, S. Keshipour, A novel electrochemical sensor for the determination of cadmium ions based on nitrogen-enriched carbon modified electrode, Sci. Rep. 15 (1) (2025) 441, http://dx.doi.org/10.1038/s41598-024-84185-7.

[29] M. Nodehi, M. Baghayeri, H. Arbabi, S. Khosrojerdi, Electrochemical sensor based on Co3O4 and Au nanoparticles for simultaneous determination of As3+ and Hg2+ by stripping voltammetry, Sci. Rep. 15 (1) (2025) 41317, http://dx.doi.org/10.1038/s41598-025-25076-3.

[30] S. Hu, S. Zhang, J. Qin, K. Cai, C. Peng, L. Luo, Y. Gu, Y. Mei, Simultaneous determination of lead and cadmium in water by metal oxide framework complex-modified glassy carbon electrodes, Microchem. J. 205 (2024) 111154, http://dx.doi.org/10.1016/j.microc.2024.111154.

[31] J.E. Vilasó-Cadre, I.A. Reyes-Domínguez, J.G. González-Fontanet, J. Hidalgo-Viteri, L.A. González-Fernández, M. de los Ángeles Arada-Pérez, G.L. Turdean, Voltammetry and related electrochemical methods based on low-cost instrumentation: a review from basic to advanced, J. Anal. Chem. 79 (2024) 520–539, http://dx.doi.org/10.1134/S1061934824050150.

[32] S. Wakhid, R. Sarno, S.I. Sabilla, The effect of gas concentration on detection and classification of beef and pork mixtures using E-nose, Comput. Electron. Agric. 195 (2022) 106838, http://dx.doi.org/10.1016/j.compag.2022.106838.

[33] M. Malikhah, R. Sarno, S.I. Sabilla, Ensemble learning for optimizing classification of pork adulteration in beef based on electronic nose dataset, Int. J. Intell. Eng. Syst. 14 (2021) http://dx.doi.org/10.22266/ijies2021.0831.05.

[34] S.M. Alzahrani, ConvAttenMixer: Brain tumor detection and type classification using convolutional mixer with external and self-attention mechanisms, J. King Saud Univ. - Comput. Inf. Sci. 35 (2023) 101810, http://dx.doi.org/10.1016/j.jksuci.2023.101810.

[35] A. Srinivaas, N. Sakthivel, B.B. Nair, Cross domain fault diagnosis in internal combustion engines using multisensor data with transfer federated and transformer based federated transfer learning, Sci. Rep. 15 (1) (2025) 36775, http://dx.doi.org/10.1038/s41598-025-20692-5.

[36] E.-S.M. El-kenawy, A.A. Alhussan, E.A. Mattar, M. Radwan, Feature selection and hyperparameter tuning in transformer-based deep learning models for photovoltaic power forecasting using the Swordfish movement optimization algorithm (SMOA), Int. J. Electr. Power Energy Syst. 174 (2026) 111509, http://dx.doi.org/10.1016/j.ijepes.2025.111509.

[37] S. Razavi, Optimizing transformer-based learning with metaheuristic algorithms for accurate and interpretable crude oil price forecasting, J. Energy Syst. Eng. 01 (02) (2025) 51–71, http://dx.doi.org/10.22034/jese.2025.565440.1018.

[38] M. Liu, X. Cheng, Y. Cao, Q. Zhou, Blueberry remaining shelf-life prediction based on the PSO-CNN-BiLSTM-MHA model, IEEE Access (2025) http://dx.doi.org/10.1109/ACCESS.2025.3548720.

[39] W. Zhang, K. Xue, A. Yao, Y. Sun, CTRNet: An automatic modulation recognition based on transformer-CNN neural network, Electronics 13 (17) (2024) 3408, http://dx.doi.org/10.3390/electronics13173408.

[40] Y. Sha, Y. Feng, M. He, Y. Jin, S. You, Y. Ji, F. Wu, S. Liu, S. Che, Cross-modality consistency network for remote sensing text-image retrieval, IEEE J. Sel. Top. Appl. Earth Obs. Remote. Sens. (2025) http://dx.doi.org/10.1109/JSTARS.2025.3586914.

[41] P. Heidari, A. Milan, Combining K-fold cross validation with Bayesian hyperparameter optimization for accuracy enhancement of land cover and land use classification, Sci. Rep. 15 (1) (2025) 39758, http://dx.doi.org/10.1038/s41598-025-23336-w.

[42] H. Wang, H. Wang, S. Qie, C. Wang, N. Li, H. Wang, Attention-based transformer-LSTM architecture for early diagnosis and staging of early-stage Parkinson's disease using fNIRS data, Front. Aging Neurosci. 17 (2025) 1677722, http://dx.doi.org/10.3389/fnagi.2025.1677722.

[43] I.A. Usmani, M.T. Qadri, R. Zia, F.S. Alrayes, O. Saidani, K. Dashtipour, Interactive effect of learning rate and batch size to implement transfer learning for brain tumor classification, Electronics 12 (4) (2023) 964, http://dx.doi.org/10.3390/electronics12040964.

[44] X. Pang, P. Yu, C. Yin, W. Liu, Z. Zheng, Transformer and bidirectional gated recurrent unit hybrid network with attention mechanisms for lithium-ion battery state-of-health estimation, J. Power Sources 658 (2025) 238370, http://dx.doi.org/10.1016/j.jpowsour.2025.238370.

[45] Y. Xiaochen, L. Qicheng, Parallel algorithm of improved FunkSVD based on GPU, IEEE Access 10 (2022) 26002–26010, http://dx.doi.org/10.1109/ACCESS.2022.3156969.

[46] A.T. Haryono, R. Sarno, K.R. Sungkono, Transformer-gated recurrent unit method for predicting stock price based on news sentiments and technical indicators, IEEE Access 11 (2023) 77132–77146, http://dx.doi.org/10.1109/ACCESS.2023.3298445.

[47] A.T. Haryono, R. Sarno, K.R. Sungkono, Stock price forecasting in Indonesia stock exchange using deep learning: A comparative study, Int. J. Electr. Comput. Eng. (IJECE) 14 (1) (2024) 861–869, http://dx.doi.org/10.11591/ijece.v14i1.pp861-869.

[48] D. Ruggeri, L. Vidács, KFold cross-validation and early stopping in foodomics neural networks: Practices, pitfalls, and recommendations, IEEE Access (2025) http://dx.doi.org/10.1109/ACCESS.2025.3623015.

[49] H. Li, G.K. Rajbahadur, D. Lin, C.-P. Bezemer, Z.M. Jiang, Keeping deep learning models in check: A history-based approach to mitigate overfitting, IEEE Access 12 (2024) 70676–70689, http://dx.doi.org/10.1109/ACCESS.2024.3402543.

[50] M. Assiri, M.M. Selim, Gesture recognition for hearing impaired people using an ensemble of deep learning models with improving Beluga whale optimization-based hyperparameter tuning, Sci. Rep. 15 (2025) 21441, http://dx.doi.org/10.1038/s41598-025-06680-9.

[51] D. Aulia, R. Sarno, S.C. Hidayati, M. Rivai, Optimization of the electronic nose sensor array for Asthma detection based on genetic algorithm, IEEE Access 11 (2023) 74924–74935, http://dx.doi.org/10.1109/ACCESS.2023.3291451.

[52] L. Muflikhah, I. Cholissodin, N. Widodo, F.E. Hermanto, T.L. Wargasetia, H. Ratnawati, R. Sarno, Single nucleotide polymorphism based on hypertension potential risk prediction using LSTM with Adam optimizer, Indones. J. Electr. Eng. Comput. Sci. 33 (2024) 1126–1139, http://dx.doi.org/10.11591/ijeecs.v33.i2.pp1126-1139.

[53] Y. On, S. Kim, S. Kim, Multi-objective optimization for design of an agrophotovoltaic system under non-dominated sorting genetic algorithm II, Comput. Electron. Agric. 224 (2024) 109237, http://dx.doi.org/10.1016/j.compag.2024.109237.

[54] H. Chang, J. Yang, Z. Wang, G. Peng, R. Lin, Y. Lou, W. Shi, L. Zhou, Efficiency optimization of energy storage centrifugal pump by using energy balance equation and non-dominated sorting genetic algorithms-II, J. Energy Storage 114 (2025) 115817, http://dx.doi.org/10.1016/j.est.2025.115817.

[55] Z. Song, C. Ren, Z. Meng, An adaptive differential evolution with opposition-learning based diversity enhancement, Expert Syst. Appl. 243 (2024) 122942, http://dx.doi.org/10.1016/j.eswa.2023.122942.

[56] O. Bilal, S. Asif, M. Zhao, Y. Li, F. Tang, Y. Zhu, Differential evolution optimization based ensemble framework for accurate cervical cancer diagnosis, Appl. Soft Comput. 167 (2024) 112366, http://dx.doi.org/10.1016/j.asoc.2024.112366.

[57] C. Zhong, G. Li, Z. Meng, Beluga whale optimization: A novel nature-inspired metaheuristic algorithm, Knowl.-Based Syst. 251 (2022) 109215, http://dx.doi.org/10.1016/j.knosys.2022.109215.

[58] P. Anilkumar, P. Venugopal, An adaptive multichannel DeepLabv3+ for semantic segmentation of aerial images using improved Beluga whale optimization algorithm, Multimedia Tools Appl. 83 (15) (2024) 46439–46478, http://dx.doi.org/10.1007/s11042-023-17247-z.

[59] R. Taori, A. Dave, V. Shankar, N. Carlini, B. Recht, L. Schmidt, Measuring robustness to natural distribution shifts in image classification, in: Proceedings of the 34th International Conference on Neural Information Processing Systems, NIPS '20, Curran Associates Inc, Red Hook, NY, USA, 2020, URL https://dl.acm.org/doi/10.5555/3495724.3497285.